

Direct Selective Laser Sintering of Superalloys

Fritz Klocke and Christian Wagner
Fraunhofer-Institute of Production Technology IPT
Aachen, Germany

Abstract

The advantages of powder metallurgy lie within the large degree of freedom for material design and thus is especially used in the production of high performance parts. Layer manufacturing is an appropriate method to produce complex parts rapidly. Direct Selective Laser Sintering (SLS) presents a technology which combines both benefits. Therefore many efforts are done today to qualify new materials for SLS [DAS 98, MEI 99, OVE 01, WOL 00]. Particular materials, which are hard to cut, to cast or to shape in any else matter, are of interest.

In the presented paper investigation results on Selective Laser Sintering of metals are shown on the basis of the nickel base alloy INCONEL™ 718. First, a process model has been created to describe the mechanisms of SLS of metals. On the base of the model, process simulations and experimental investigations have been performed. In some cases, affiliating a heat treatment after the laser sintering step is favorably to improve the metallic structure and thus has also been tested. Finally, the metallographic structures and mechanical properties were analysed.

1. Introduction

In Selective Laser Sintering of high performance metals, two bad effects have been observed: balling and oxydation. During process observation, it was found that materials without a semisolid phase, like pure metals, show strong balling effects, whereas alloys with a semi-solid phase are better to process. Therefore it was assumed, that metal droplets in a superliquid state tend to flow together abruptly and in a semisolid phase the fusion process lasts longer, which is benefical for the SLS process. If this theses would apply, the most important job during SLS would be to heat the process zone exactly between the liquidus and solidus temperature, when processing technical alloys.

To verify the theses, first a base test with two metal grains was done. Then a process model, which enables the prediction process parameters, was developed. The process model was the base for an FEM-simulation of SLS. It also gives hints for process boundary conditions, like maximum oxygen contents in process atmosphere. The results and conclusions were used to build sample parts of IN 718.

2. Base test: sintering behaviour of 2 grains

The objective of this test was to determine the melting behaviour and fusion velocity of semisolid and non-semisolid metals. The test constallation of the 2-grain test is shown in **fig. 1a**). Two grains were positioned side by side on a polished aluminium plate. A laser beam with controlled power P, which has been varied during testing from 125 W to 20W, and was occuring vertically during a exposure time $t_{exp.} = 1000$ ms on the particles. The objective was to observe how long the fusion time $t_{sint.}$ lasts for different laser powers. For the description of the sintering stage, the coalescence ratio S was introduced, see **fig. 1b**).

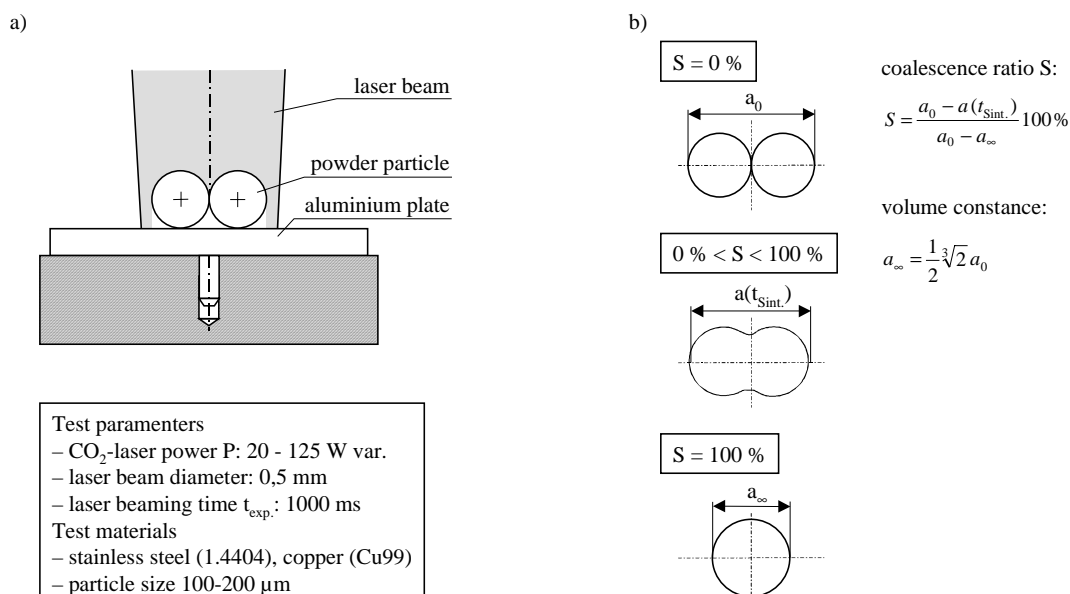


Fig. 1: a) test set-up and test programme; b) explanation of introduced test dimensions

The process was recorded with a high speed camera with a picture frequency of 2000 Hz. Tested materials have been copper of 99 % purity (Cu99) and stainless steel 1.4404. Copper has its melting point at $T_{\text{melt}} = 1083 \text{ }^{\circ}\text{C}$, whereas the stainless steel starts to melt at $T_{\text{sol.}} = 1375 \text{ }^{\circ}\text{C}$ and is completely molten at $T_{\text{liq.}} = 1430 \text{ }^{\circ}\text{C}$, see **table 1**.

material	composition [%]	T_{solid}	T_{liquid}	$\Delta T_{\text{liquid-solid}}$
copper Cu99	Cu div. elements 99 bal.	–	1083 °C	0 °C
stainless steel 1.4404	C Cr Ni Mo Mn Si Fe 0,03 17 12 2,5 <2 <1 bal.	1375 °C	1430 °C	55 °C
nickel base alloy IN 718	C Cr Ni Mo Mn Si 0,08 21 55 3 0,35 0,35 Al B Nb Ti Fe 0,6 0,004 5 1 bal.	1300 °C	1365 °C	65 °C

Table 1: Chemical composition and melting temperatures of tested materials [ROE 69, SCU91, INC 85]

In **fig. 2**, two series of high speed recordings of the tests are shown. In the tests, two different coalescence behaviours have been observed: copper always melts abruptly, regardless of the laser power, **fig. 2a**). The fusion times for copper are nearly the same at all tested powers and amount all to 1,5 until 2,5 ms. The coalescence behaviour of stainless steel is different: the sintering time of stainless steel 1.4404 depends on the laser power P , see **fig. 3**. The coalescence ratio S has been determined by evaluating the high speed photographs from the tests. For laser powers of 50 W and up, that the fusion times $t_{\text{sint.}}$ to complete coalescence ($S = 100 \%$) are all very short ($t_{\text{sint.}} < 5\text{ms}$). In **fig. 2b**), the coalescence process of stainless steel for a laser power of 30 W is shown. The final stage is reached within approx. 40 ms. With decreasing laser power P , the coalescence time $t_{\text{sint.}}$ grows. The fusion times for 1.4404 range from 2 ms to approx. 70 ms.

Referring to these observations, the theses of the sintering in the semisolid stage is applying: in the semisolid state, the viscosity is higher than in the superliquid state and the fusion duration is longer. In **fig. 3**, the curves of copper are not included. They have all the same formation and can be compared to the stainless steel graph for $P = 125 \text{ W}$. The laser power of 40 W, which has been applied in the test in **fig. 2a**), is also the lowest power, where sintering of copper occurs.

IN 718 has not been included in the 2 grain test, but it is assumed that the results can be transferred from 1.4404 to other semisolid alloys. A justification for this assumption is seen in the fact, that both tested materials, Cu99 and 1.4404, flow together within the same time ($\approx 2\text{ms}$), when being superliquid. On the other hand, the superliquid viscosity μ of a Fe-Cr20-Ni10,5 alloy amount to 9,2 mPa·s at 1500 °C, whereas Cu has viscosity of 3 mPa·s at 1100 °C [KAW 88]. As a result, a difference in viscosity within this order of magnitude has no big impact. The viscosity in the semisolid range, which is considered as a decisive factor, must be tremendously higher than in the superliquid area.

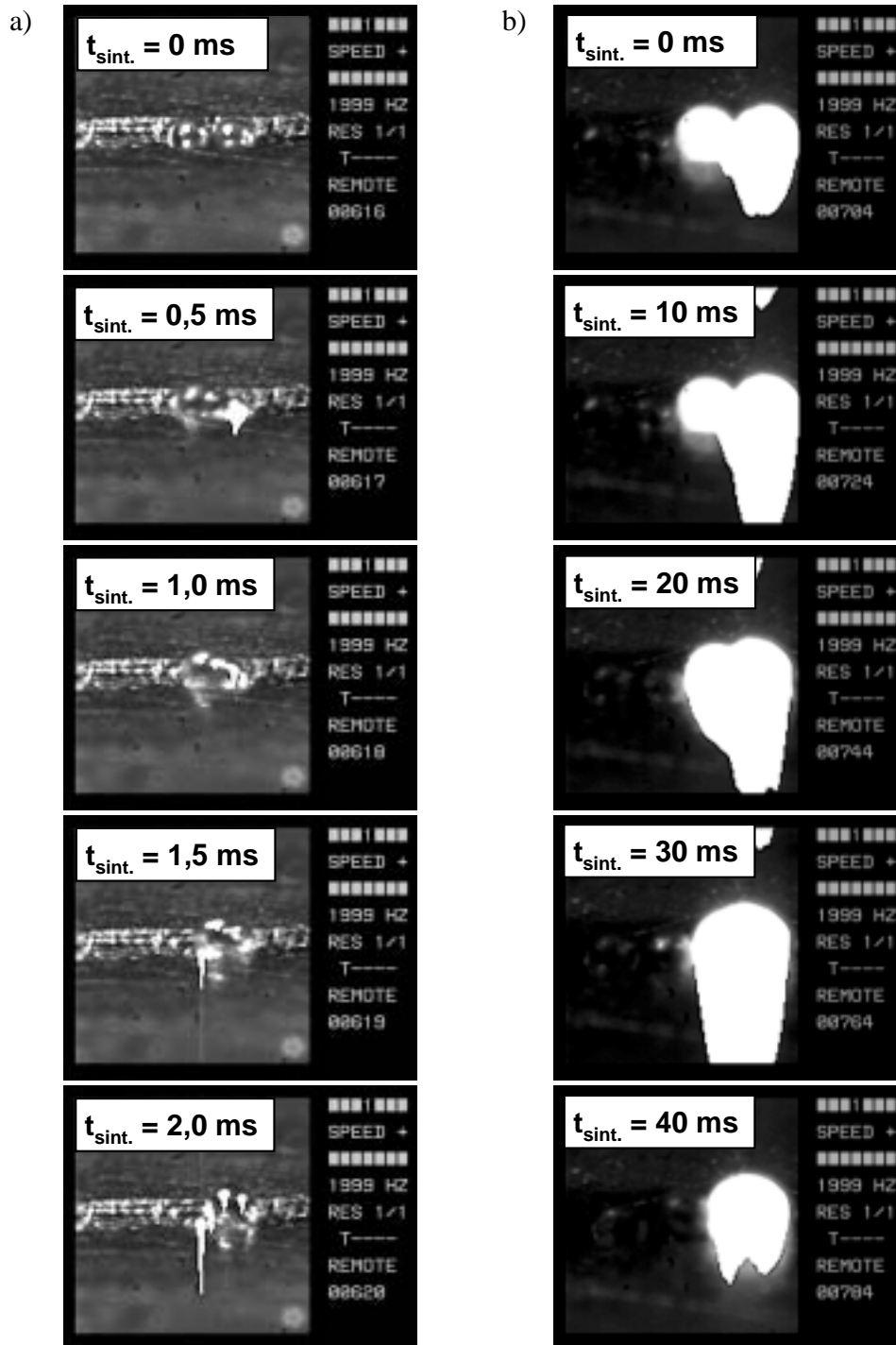


Fig. 2: High speed recordings of the 2-grain tests: a) Copper Cu99, $P = 40$ W; b) stainless steel 1.4404, $P = 30$ W

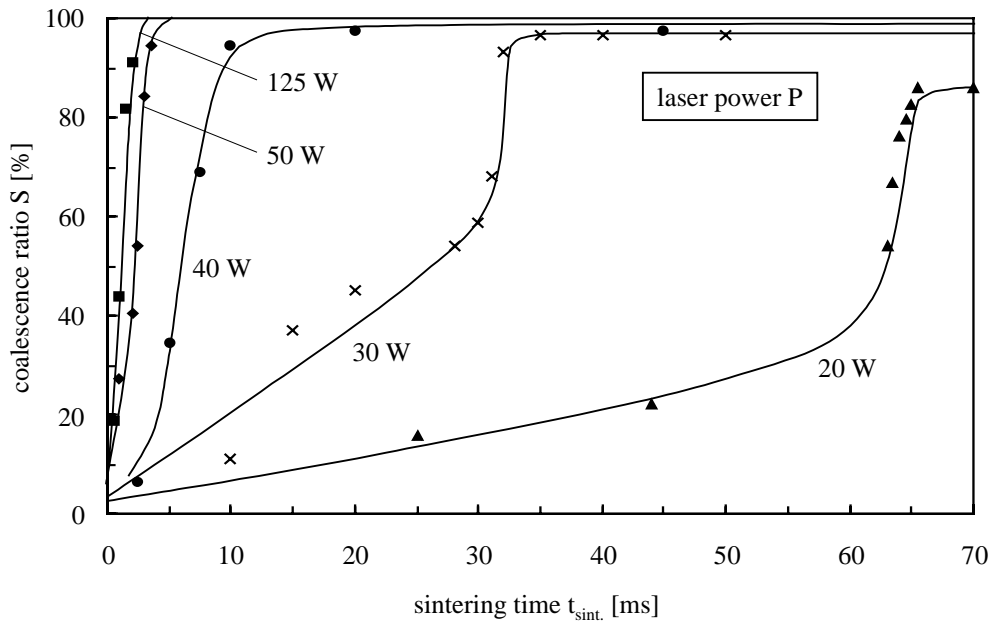


Fig. 3: Coalescence times for 2 stainless steel particles in dependence of the laser power P

3. Modeling of SLS

With respect to the 2-grain test results, the temperature field during SLS should be kept between $T_{sol.}$ and $T_{liq.}$ within the actual powder layer and slightly below. For that purpose, a process model has been created to calculate the temperature distribution within the process zone. The base of this model is a standard material cell which represents the typical material behaviour of the powder bed during SLS. The material properties and physical procedures during laser sintering can be sorted to 4 different categories: the thermal sub-process, the metallurgical sub-process, the chemical sub-process and the sintering sub-process. Each of these 4 processes was treated separately at first. After that the submodels had been composed to an integrated process model.

3.1 The thermal submodel

The thermal submodel includes all thermal dimensions of the process, e.g. the specific heat c_p and the thermal conductivity λ . Both properties are temperature dependent. Tabled values of c_p and λ for a large range of technical alloys can be found in [VDI 97]. The specific heat is only a function of the temperature, whereas the thermal conductivity is a function of the temperature and the contact interface between the particles. The latter could also be expressed by the relative density $\rho_{rel.}$ as will be demonstrated later. The basic equation for the heat transfer problem is then:

$$\rho(\rho_{rel.})c_p(T)\frac{\partial T}{\partial t} = \lambda(T,\rho_{rel.})\frac{\partial^2 T}{\partial \vec{n}^2} \quad \text{eq. 1}$$

For powder beds during laser sintering, ρ is a function of the void fraction respectively of the relative density $\rho_{rel.}$. Due to the dependancies in eq. 1, the heat transfer problem becomes non-linear and can only be solved by numerical methods.

The thermal submodel also includes the definition of the heat source term, which has to be added to eq. 1. Two important factors in defining the heat source are the laser energy absorption and optical penetration depth. The absorption grade A has been measured by the method of diffuse reflection (DR) with an FT-IR spectrometer 1700X from Perkin-Elmer Ltd.. It was determined to 18-20% for IN 718. For the calculations, the value was set to $A = 0,2$. The optical penetration depth $\delta_{opt.}$ for metals is rather low with $42 \text{ nm} < \delta_{opt.} < 106 \text{ nm}$ for a temperature range of $300 \text{ K} < T < 1800 \text{ K}$ [HOF 93]. Therefore a surface heat source can be considered when calculating laser assisted heat-up procedures of metals. To take into account the penetration in the powder bed through the particle gaps, a penetration factor of $\delta'_{opt.} = 0,15 \text{ }\mu\text{m}$, which is half of the average diameter of the powder particles, was included. The equation for a laser beam with gaussian energy distribution as volumetric heat source becomes then:

$$q(x, y, z) = -\frac{A}{\delta'_{opt.}} I_0 \exp\left(-2\frac{x^2 + y^2}{r_b^2} - \frac{z}{\delta'_{opt.}}\right), \quad \text{eq. 2}$$

where I_0 is the intensity in the beam center and r_b the beam radius.

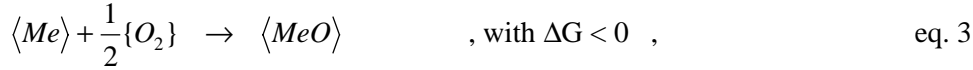
Also the latent heat $H_{melt.}$ of the crystalline metal material is considered in the calculations. The exact value for IN 718 has been unknown, so that the latent heat for nickel was taken $H_{melt.(Ni)} = 289 \text{ J/g}$. In the calculations, a linear assignment of the melting energie between $T_{sol.}$ and $T_{liq.}$ was assumed.

3.2 The metallurgical submodel

This submodel considers the metallurgical material properties of the metal, e.g. the solidus and liquidus temperature $T_{sol.}$ and $T_{liq.}$ or the values of the latent heat of melting or of lattice transformation. The metallurgical submodel is also important for explanations of the processes in the cooling period and the resulting metallic structure. The metallurgical process might become even more relevant, if the process of melting and the refering viscosity in the semisolid state would be investigated in more detail. When studying laser sintering of powder mixtures, the process of microalloying also requires metallurgical modelling by means of phase diagramms.

3.3 The chemical submodel

The chemical submodel describes every process of chemical material transformation. The most important and worst reaction for metal laser sintering is oxydation. Oxyde skins prevent proper sintering and wetting [SCH 92]. The general reaction equation for a metal oxydation is:



where ΔG is the free enthalpy. If ΔG is ≥ 0 , the oxydation is impossible, if ΔG is < 0 , the oxydation could happen. The bigger the absolute value of ΔG is, the more likely the reaction is. The free enthalpy can be calculated from

$$\Delta G = \Delta G^0 + RT \ln \frac{1}{p_{O_2}^{1/2} \cdot a_{Me}} = -RT \ln K_{MeO} + RT \ln \frac{1}{p_{O_2}^{1/2} \cdot a_{Me}} < 0 \quad \text{eq. 4}$$

Values of the free creation enthalphy ΔG^0 and of the equilibrium constant K for a large variety of elements and bondings can be found in [BAR 73]. When an element is present in a diluted form, like in alloys, the chemical reactivity, expressed by the activity a , changes. For alloys containing many elements, like for example for IN 718, the acticity a_{Me} of each element can be set to 1. The graphs for metals and the referring oxygen partial pressures can be derived from an Richardson-Ellingham diagram [FRO 94]. For IN 718 the most critical element is aluminium. Following the Richardson-Ellingham diagram, the partial pressure of oxygen p_{O_2} must be less than 10^{-25} atm to prevent oxydation.

3.4 The sintering submodel

The sintering submodel includes mainly rheological processes. One aim is to determine the differential equation of the fusion process of two plastified particles, depending on the surface tension and viscosity. Another objective is the transfer of the base case of two particles to a package of more particles. The purpose of the sintering submodel is also to explain clustering of particles during sintering (balling effect).

The inital powder bed density has been deterrmind to $\rho_{rel.(IN\ 718)} = 0,55$. Following the 2-grain tests, the powder bed becomes fully dense within 2 ms in zones where the temperature exceeds $T_{liq.}$. The sintering stage and the referring relative density and contact area is dependent on temperature and time. To mount an equation of the kind $\rho_{rel.}(T, t)$, more detailed investigations of isothermal sintering rates would be necessary. For the calculation carried out here, a linear raise of the relative density from 0,55 to 1 in the heat-up period from $T_{liq.}$ to $T_{sol.}$ has been assumed.

For the thermal conductivity, the size of the contact interface of the particles is relevant. The contact between the powder particles is setting the conductive cross section of the material continuum. It ranges from a point contact of the spheric particles to a 100% contact, see **fig. 4**. In measurements, the thermal conductivity λ of the powder bed has been determined after the laser flash analysis (LFA) method using a LFA 427 system from the Netzsch GmbH. At room temperature, it was found that $\lambda_{powder\ (IN\ 718)}(20\ ^\circ C)$ is less than 1 W/mK. The value for compact IN 718 material is $\lambda_{(IN\ 718)}(20\ ^\circ C) = 13$ W/mK and for $T_{sol.}$ approx. $\lambda_{(IN\ 718)}(1200\ ^\circ C) = 33$ W/mK [VDI 97]. Thus, λ has been set to:

$$\begin{aligned}
T < T_{sol.}: & \quad \lambda = 1 \frac{W}{mK} \\
T_{sol.} < T < T_{liq.}: & \quad \lambda = \left(1 + \frac{T - T_{sol.}}{T_{liq.} - T_{sol.}} 32\right) \frac{W}{mK} \\
T > T_{liq.}: & \quad \lambda = 33 \frac{W}{mK}
\end{aligned}$$

3.5 The integrated model

The above mentioned subprocesses have been consolidated to a complete model. For this consolidation, a standard material cell has been created, see **fig. 4**. The standard material cell was developed from a powder particle, lying in a cubic powder package. The process stages are heating-up, melting start and wetting the underlying particle, coalescence and the final stage. In the wetting stage, the underlying particle is heated up quickly by heat conduction. Finally it also melts and both are forming an sintering neck which is growing until both have flown together completely, which is the final stage. This cell model has been used to simulate the material behaviour in the powder bed during laser sintering, but it does not consider balling and clustering effects. These mechanisms have to be modelled additionally and might be subject of future investigations.

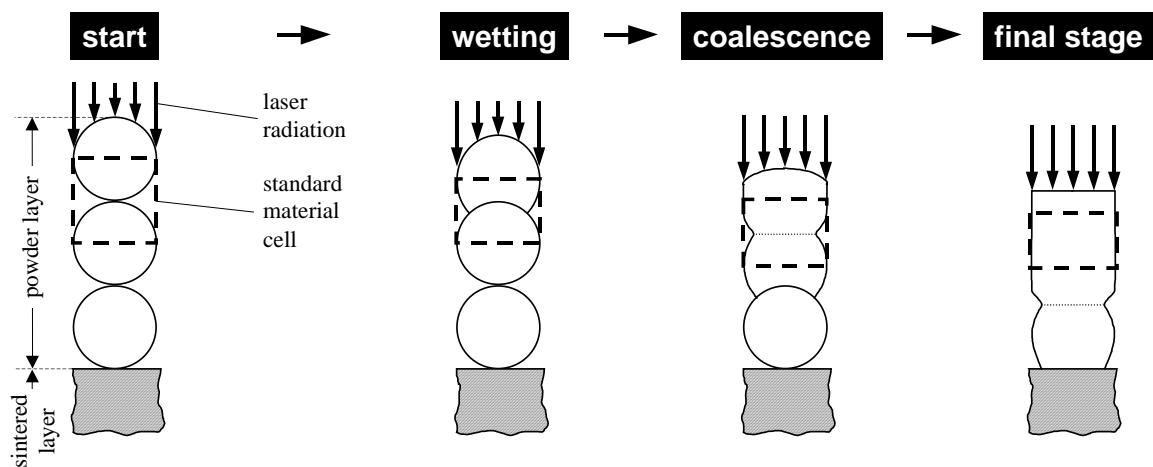


Fig. 4: Model of the standard material cell

4. FEM-Simulation

By use of the standard material cell, a simulation of the powder bed has been made by a FEM calculation for a laser pulse scanning. In **fig. 5a**), the FEM model which represents the scanning of one powder layer on a sintered structure is illustrated. In the setup, the corner of a cube is radiated with a laser beam pulse of the power P for the exposure time $t_{exp.}$. The cube itself consists of a $50 \mu\text{m}$ thick powder layer on the surface and with a solid of the same material underneath. Originally, the laser beam has a round shape (diameter $0,5 \text{ mm}$) and gaussian energy distribution. The beam hits the cube with a quarter circle. In the calculations, the laser power P and exposure time $t_{exp.}$ have been varied. From the

exposure times, the referring scanning velocities v can roughly be calculated by the relation $v = r_B/t_{exp.}$. In **fig. 5b)**, the results for IN 718 are shown for three different parameter sets, e.g. $P = 200 \text{ W}/t_{exp.} = 5,9 \text{ ms}$, $P = 170 \text{ W}/t_{exp.} = 10 \text{ ms}$ and $P = 125 \text{ W}/t_{exp.} = 50 \text{ ms}$.

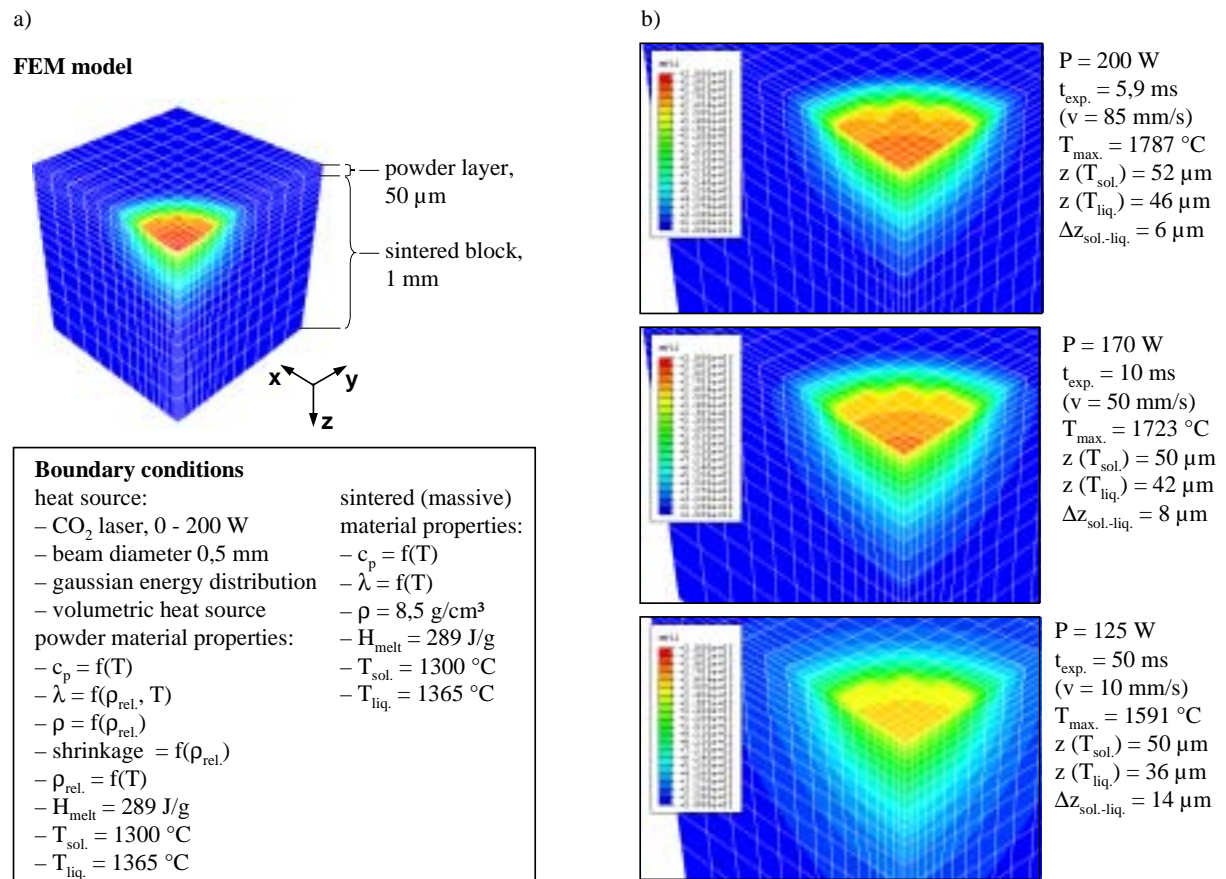


Fig. 5: a) FEM model configuration and boundary conditions; b) process simulation for IN 718

From the calculations in **fig. 5b)** it can be concluded, that scanning with low velocities and adapted low laser powers is more suited for laser sintering. With decreasing P and v , the maximum temperatures $T_{max.}$ become lower and the semisolid area $\Delta z_{sol.-liq.}$ widens up. With the calculations the parameters of technical alloys can be derived. For IN 718, the parameter set $P = 125 \text{ W}/v = 10 \text{ mm/s}$ is supposed to be the best from those in fig. 5. If the process should be speeded up by increasing the scanning velocity, a decrease of the layer thickness would be necessary.

5. SLS results of INCONEL 718

On testing the nickel base alloy INCONEL 718 with SLS, sample cubes with the dimension 10x10x10 mm³ have been fabricated first. With these samples, the hardness and the metallographic structure have been analysed. Compared with conventional fabricated IN 718, a sensible decrease in hardness could be observed, see **table 2**. Until now, no final explanation has been found but it is assumed that the short process times of SLS do not allow mixed crystal formation, which causes a hardening effect [HAA 94]. The metallic structure of SLS is very fine and grain boundaries could hardly be observed, see **fig. 6a) + b)**. The part has no visible porosity, but in some areas, failures, like pores, could be observed. A hot isostatic pressing process was considered to eliminate these failures.

	IN 718 SLS	IN 718 SLS + HIP	IN 718 conventional
Hardness (HV 0,2)	323 HV 0,2	268 HV 0,2	538 HV 0,2
Tensile strength (R_m)	–	750 N/mm ²	1430 N/mm ² *)
Fracture strain A₅	–	16,9 %	21 % *)

Table 2: Mechanical properties of differently fabricated IN 718 (*) values taken from [BEI 90])

In the next step, tensile strength test bars have been produced by SLS, hiped for 4 hours at 1150 °C and at 1900 bar and were finally machined to net shape, see **fig. 6c)**. The tensile test results are presented in **table 2**. The strength of the laser sintered structure of 750 N/mm² is quite low, compared with conventional IN 718. In the analysis of the test bars after the tensile tests, clusters of refractory oxides were found in the metallic structure, which itself is very ductile. It can also be seen that the deformation of the bars is caused by delamination. However, it is concluded, that oxydation during SLS and remaining, thin oxide skins on the SLS layers are the main reasons for the observed effects and has to be reduced intensely in future activities.

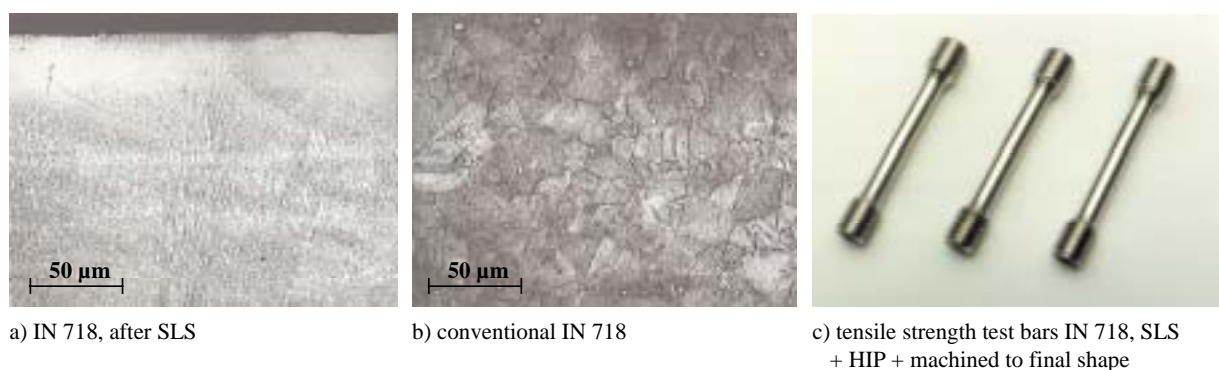


Fig. 6: a) + b) micrographs of grinded and etched IN 718 structures; c) tensile strength test bars (length 65 mm, M10, diameter 6mm)

6. Summary and outlook

On a base test, the general coalescence behaviour of 2 metal grains was investigated. From the realised difference between semisolid and non-semisolid materials, it was concluded that process temperatures between $T_{\text{sol.}}$ and $T_{\text{liq.}}$ within the actual powder layer are beneficial to achieve satisfying process results. To permit temperature control, a process model for SLS was developed. It includes 4 submodels, e.g. the thermal, the metallurgical, chemical and sintering submodel. It can be used to predict or estimate process parameters, especially the combination of laser power, scanning velocity and layer thickness. The model has been applied for the nickel base alloy INCONEL™ 718 by means of an FEM simulation and practical tests. It was possible to fabricate cubic sample parts for metallurgical analysis and bars for tensile strength testing. The mechanical strength of the material was not satisfying which is attributed to a high oxygen content in the material.

Future work aims on machine and process modifications to reduce the oxygen content of laser sintered samples. Also the combination of laser power, scanning velocity and layer thickness has still not been optimised yet. Another important subject of investigations is seen in the thermal post treatment.

7. Literature

- [BEI 90] Beitz, W., Kuettner, K.H.; Dubbel – Taschenbuch fuer den Maschinenbau; 17th edition, Springer Verlag, Berlin-Heidelberg-New York, 1990
- [DAS 98] Das, S.; Direct Selective Laser Sintering of High Performance Metals – Machine Design, Process Development and Process Control; ; The University of Texas at Austin, Austin/Texas, PhD. Dissertation, 1998
- [FRO 94] Froberg, M.; Thermodynamik fuer Werkstoffingeniuere und Metallurgen; 2th edition, Deutscher Verlag fuer Grundstoffindustrie, Stuttgart/Germany, 1994
- [HAA 94] Haasen, P.; Physikalische Metallkunde; 2th edition, Springer Verlag, Berlin-Heidelberg-New York, 1994
- [HOF 93] Hoffmann, C., Untersuchung des Waermetransports beim Haerten und Schneiden mit Laserstrahlung; RWTH Aachen/Germany, Dissertation, 1991
- [INC 85] N.N., INCONEL™ 718, product information from Inco Alloys International Inc., 4th edition, 1985
- [KAW 88] Kawai, Y, Shiraishi, Y; Handbook of Physio-chemical Properties at High Temperatures; The Iron and Steel Institute of Japan, Tokyo/Japan, 1988
- [MEI 99] Meiners, W.; Direktes Selektives Lasersintern einkomponentiger metallischer Werkstoffe ; RWTH Aachen/Germany, Dissertation, 1999
- [OVE 01] Over, C. et al.; Selective Laser Melting: A new Approach for the Direct Manufacturing of Metal Parts and Tools; Proceedings of the LANE, 2001
- [ROE 69] N.N., Internal Investigations of Roechling Burbach AG, 1969, Voelklingen/Germany
- [SCH 92] Schatt, W.; Sintervorgaenge; VDI-Verlag GmbH, Duesseldorf/Germany, 1992

- [SCU 91] H. Schumann; Metallographie; Deutscher Verlag fuer Grundstoffindustrie, Stuttgart/Germany, 13th edition, 1991
- [VDI 97] N.N., VDI-Waermeatlas, 8th edition, Springer Verlag, Berlin-Heidelberg, 1997
- [WOL 00] Wohlerl, M.S.; Hot Isostatic Pressing of Direct Selective Laser Sintered Metal Components; The University of Texas at Austin, Austin/Texas, PhD. Dissertation, 2000